

Letter

Evidence of non-Solar elemental composition in the clocked bursts from SRGA J144459.2–604207

Akira DOHI^{1,2}, Nobuya NISHIMURA^{3,1,4}, Ryosuke HIRAI^{1,5,6}, Tomoshi TAKEDA^{7,1}, Wataru IWAKIRI^{8,1}, Toru TAMAGAWA¹, Amira AOYAMA^{7,1}, Teruaki ENOTO^{9,1}, Satoko IWATA^{7,1}, Yo KATO¹, Takao KITAGUCHI¹, Tatehiro MIHARA¹, Naoyuki OTA^{7,1}, Takuya TAKAHASHI^{7,1}, Sota WATANABE^{7,1} and Kaede YAMASAKI^{7,1}

¹RIKEN Cluster for Pioneering Research (CPR), RIKEN, Wako, Saitama 351-0198, Japan

²Interdisciplinary Theoretical and Mathematical Sciences Program (iTHEMS), RIKEN, Wako, Saitama 351-0198, Japan

³Center for Nuclear Study (CNS), The University of Tokyo, Bunkyo-ku, Tokyo 113-0033, Japan

⁴National Astronomical Observatory of Japan (NAOJ), Osawa, Mitaka 181-8588, Japan

⁵School of Physics and Astronomy, Monash University, Clayton, VIC 3800, Australia

⁶OzGrav: The ARC Centre of Excellence for Gravitational Wave Discovery, Clayton, VIC3800, Australia

⁷Department of Physics, Tokyo University of Science, Kagurazaka, Shinjuku-ku, Tokyo 162-8601, Japan

⁸International Center for Hadron Astrophysics, Chiba University, Chiba 263-8522, Japan

⁹Department of Physics, Kyoto University, Sakyo, Kyoto 606-8502, Japan

*E-mail: akira.dohi@riken.jp

Abstract

In February and March 2024, several Type I X-ray bursts from the accreting neutron star SRGA J144459.2–60420 were detected by multiple X-ray satellites, with the first reports coming from INTEGRAL and NinjaSat. These observations reveal that after exhibiting very regular behavior as a “clocked” burster, the peak luminosity of the SRGA J144459.2–60420 X-ray bursts shows a gradual decline. The observed light curves exhibit a short plateau feature, potentially with a double peak, followed by a rapid decay in the tail—features unlike those seen in previously observed clocked bursters. In this study, we calculate a series of multizone X-ray burst models with various compositions of accreted matter, specifically varying the mass fractions of hydrogen (X), helium (Y), and heavier CNO elements or metallicity (Z_{CNO}). We demonstrate that a model with higher Z_{CNO} and/or lower X/Y compared to the solar values can reproduce the observed behavior of SRGA J144459.2–60420. Therefore, we propose that this new XRB is likely the first clocked burster with non-solar elemental compositions. Moreover, based on the X-ray burst light curve morphology in the decline phase observed by NinjaSat, a He-enhanced model with $X/Y \approx 1.5$ seems preferred over high-metallicity cases. We also give a brief discussion on the implications for the neutron star mass, binary star evolution, inclination angle, and the potential for a high-metallicity scenario, the last of which is closely related to the properties of the hot CNO cycle.

Keywords: X-rays: bursts — X-rays: binaries — stars: neutron — stars: evolution — nuclear reactions, nucleosynthesis, abundances

arXiv:2411.10993v1 [astro-ph.HE] 17 Nov 2024

1 Introduction

On 26 February 2024, new observations of Type I X-ray burst (hereafter, X-ray burst: XRB) from SRGA J144459.2–60420 (SRGA J1444), located in the Galactic disc, were reported by INTEGRAL (Sanchez-Fernandez et al. 2024) and NinjaSat (Takeda et al. 2024). Follow-up observations were conducted by several X-ray astronomical satellites, e.g., NICER (Ng et al. 2024), MAXI (Mihara et al. 2024), IXPE (Papitto et al. 2024) and Insight-HXMT (Li et al. 2024). The observed bursts from SRGA J1444 are considered to be a *clocked* burster, which shows a burst-to-burst uniform light curve profile and constant recurrence time. Thus, SRGA J1444 is the sixth confirmed clocked XRB after GS 1826–24 (Ubertini et al. 1999; Cocchi et al. 2001; Cornelisse et al. 2003; Galloway et al. 2004), GS 0836–429 (Aranzana et al. 2016), EXO 1745–248 (Matranga et al. 2017), MAXI J1816–195 (Bult et al. 2022) and 1RXS J180408.9–342058 (Wijnands et al. 2017; Fiocchi et al. 2019).

Type I XRBs are thermonuclear explosions triggered by nuclear ignition of hydrogen and helium in the accreted layer on the neutron star (NS) surface. Observations of XRBs provide various information relevant to nuclear astrophysics and the physical properties of low-mass X-ray binaries. Among more than 100 XRBs observed so far (Galloway et al. 2020), the most suitable sites for constraining the physics of low-mass X-ray binaries are the clocked bursters due to their uniform features (for a review, see Galloway et al. 2017 and references therein). Since the first modeling of the well-known clocked burster GS 1826–24 (Heger et al. 2007), observations of clocked burster light curves have been used to constrain physical properties in accreting NSs, companion stars and surface nuclear burning (e.g. Lampe et al. 2016; Meisel 2018; Meisel et al. 2019; Dohi et al. 2020; Johnston et al. 2020; Hu et al. 2021; Dohi et al. 2021; Dohi et al. 2022; Lam et al. 2022a; Lam et al. 2022b).

The main observed features of SRGA J1444 are shown in figure 1. The MAXI light curve (black) indicates a rise and fall in the persistent X-ray flux, indicating variability in the mass accretion rate over a duration of about one month (see Section 2.2). XRBs were observed during and after the peak, as indicated by the colored lines in figure 1. The bursts were periodic around the peak of the persistent flux, suggesting that SRGA J1444 is a clocked burster, with periodic recurrence times of 1.69 h (Sanchez-Fernandez et al. 2024). In the later phase, the luminosity of the SRGA J1444 bursts gradually decline, and the recurrence time increases, as observed by IXPE (Papitto et al. 2024) and NinjaSat (Takeda et al. 2025). Takeda et al. (2025) observed the successfully observed 11 burst events for around two weeks in the decline phase, with the last two occurring consecutively, separated by $\Delta t = 7.909$ h. Unlike other typical clocked bursters, such as GS 1826–24 (Galloway et al. 2017), the bursts in SRGA J1444 exhibit a plateau peak, possibly featuring a double peak, followed by a rapid decay with an exponential decay timescale of $\tau_e \sim 9$ s (figure 1b and see also Ng et al. 2024).

In the present study, we theoretically investigate SRGA J1444 to constrain the physical properties of the low-mass X-ray binary system. We calculate a series of multizone XRB models using a 1D spherically symmetric general relativistic stellar evolution code, HERES (Dohi et al. 2020). With representative mass accretion rates, we compare our models with a variety of elemental *compositions* of the accreted matter, i.e., hydrogen (X), helium (Y), and heavier CNO elements or metallicity (Z_{CNO}). The model with higher Z_{CNO} and lower X/Y compared to the solar compositions can reproduce the observations, including the recurrence time Δt

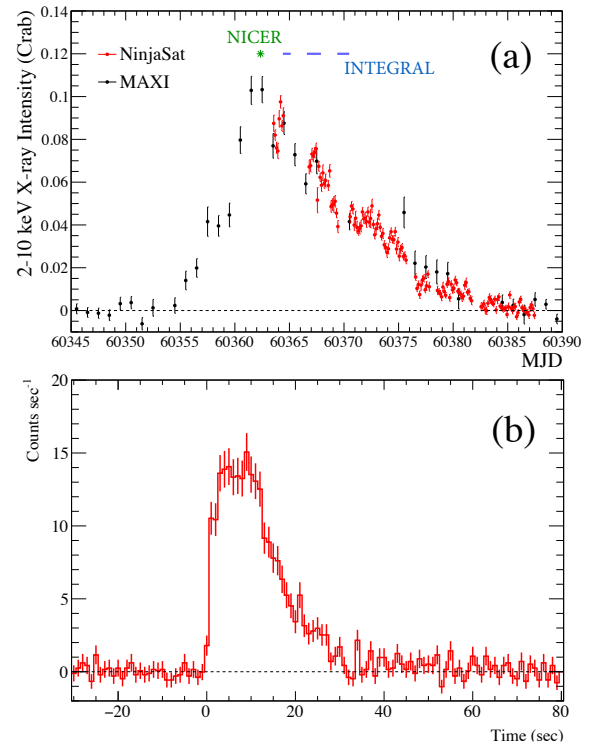


Fig. 1. (a) Simultaneous persistent-flux observations of the SRGA J1444 with various X-ray detectors. The time-bin width is 3 h for MAXI and 3 h for one day. (b) The averaged burst profile observed by NinjaSat.

with appropriate choices of the accretion rate.

This paper is structured as follows: In Section 2, we summarize the numerical methods for XRB calculations, including the initial conditions and the adopted binary parameters. The results are presented in Section 3. Section 4 provides a summary and discussion.

2 Methodology: XRB modeling

2.1 XRB code: HERES

In modeling the theoretical light curves of SRGA J1444, we utilize a general relativistic stellar evolution code, HERES (Hydrostatic Evolution of RELativistic Stars) described in Fujimoto et al. (1984) and Dohi et al. (2020), which simultaneously solves the Tolman-Oppenheimer-Volkof equation along with the thermal transport equation, accounting for nuclear burning and neutrino cooling. The validity of HERES has been thoroughly verified by comparing its results with those of MESA models (Zhen et al. 2023). It should be noted that SRGA J1444 does *not* exhibit photospheric radius expansion, allowing us to safely apply HERES modeling.

The HERES code solves the thermal evolution of accreting NSs, considering realistic EOSs and heating and cooling sources. We adopt the Togashi EOS (Togashi et al. 2017), which has been constructed with realistic nuclear potentials at finite temperature, specifically for $1.4 M_{\odot}$ NSs (with a radius of 11.6 km). Regarding NS cooling, we consider “slow neutrino cooling processes”, mainly composed of the modified Urca process and Bremsstrahlung. Note that fast neutrino cooling processes, such as the Direct Urca process, are prohibited with the Togashi EOS (Dohi et al. 2019). For the heating in the NS crust, which consists of electron capture, neutron emission, and pycnonuclear fusion,

we adopt the standard heating rates (Haensel & Zdunik 2008) to describe their energy generation.

Explosive nuclear-burning phases in the burst regimes are solved with a nuclear reaction network coupled with the hydrostatic evolution. Our approximated reaction network is only valid for $X/Y \gtrsim 1$, which satisfies our current parameter space. At the typical XRB density of $\rho \sim 10^6 \text{ g cm}^{-3}$, burning processes proceed from the triple- α reaction, through the hot CNO (bi-)cycle, and into the αp and rp processes (Meisel et al. 2018, for a review). To efficiently cover all nucleosynthesis processes, we implement an approximate reaction network with 88 nuclei, ranging from n/p to ^{107}Te (see Dohi et al. 2020 for details). All relevant reaction rates are sourced from JINA Reaclib. Note that our previous studies, such as Dohi et al. 2021, used JINA Reaclib version 2.0. Both versions are available in the JINA Reaclib Database¹.

2.2 Accretion model parameters

Besides the physical properties of the NS, the input parameters for calculating XRBs are related to the values of the X-ray binary system, i.e., the accretion rate \dot{M}_{-9} and the composition of the accreted matter: the mass fractions of hydrogen (X), helium (Y), and metallicity (Z). For the elemental composition, we consider the hydrogen-helium ratio (X/Y), and Z is represented by the total CNO nuclei, $Z = Z_{\text{CNO}}$.

In modeling the SRGA J1444 bursts, we distinguish two phases. The first phase is the clocked burst phase, corresponding to the phase with high persistent flux (~ 0.1 Crab). In this paper, we take the information of INTEGRAL of $\Delta t \simeq 1.69$ hr and $\tau_e \simeq 9$ s, and the light curves by NICER, available under ObsID 6204190102 and previously analyzed in Ng et al. (2024). The NICER data were processed using NICERDAS version 11 as distributed with HEASOFT version 6.32. The second phase is where the persistent luminosity of SRGA J1444 gradually declines, corresponding to when the NinjaSat and IXPE observations were taken. In the NinjaSat observations, the 10th and 11th XRBs occur consecutively, which gives $\Delta t = 7.909$ hr (Takeda et al. 2025). For the light curves, we take the averaged profile of the 10th and 11th XRBs, assuming a bin size of 1 s. The light curve by NinjaSat is calculated in the 2-20 keV energy band after subtracting persistent emission.

The mass accretion rate can be roughly estimated from the persistent flux by relating it to the gravitational energy release of the accreted matter. In our models, we adopt $\dot{M}_{-9} = 3$ and 4 for the clocked burst phase with the mass accretion rate \dot{M}_{-9} in units of $10^{-9} M_{\odot} \text{ yr}^{-1}$. In the later phase, the persistent flux counts are insufficient to constrain the accretion rate, so we use the empirical relation between the accretion rate and XRB recurrence time

$$\dot{M}_{-9} \propto \Delta t^{-\eta} \quad (1)$$

where the parameter η is close to 1 (e.g., see Lampe et al. 2016). In the case of SRGA J1444, η is estimated to be ~ 0.8 (Ng et al. 2024; Takeda et al. 2025). From the observed Δt , one can constrain the accretion-rate ratio between the clocked phase and the later phase observed by NinjaSat (see figure 1b) as roughly

$$\frac{\dot{M}_{-9, \text{NinjaSat}}}{\dot{M}_{-9, \text{clocked}}} = \left(\frac{\Delta t_{\text{clocked}}}{\Delta t_{\text{NinjaSat}}} \right)^{\eta} \simeq 0.2 - 0.25, \quad (2)$$

where $\dot{M}_{-9, \text{clocked}}$ and $\dot{M}_{-9, \text{NinjaSat}}$ are the mass accretion rates at the clocked phase and the later phase observed by NinjaSat,

respectively. Based on the constraint of equation (2), we adopt $\dot{M}_{-9} = 0.8$ and 0.9 for the modeling of NinjaSat light curves.

In contrast to the accretion rate \dot{M}_{-9} , we adopt common values for the composition in both phases. In this study, we focus on the impact of composition by considering three cases: (i) the solar composition, with $X/Y = 2.9 \equiv (X/Y)_{\odot}$ and $Z_{\text{CNO}} = 0.015 \equiv Z_{\odot}$, (ii) He-enhanced case, with $X/Y = 1.5 \simeq (X/Y)_{\odot}/2$ and $Z_{\text{CNO}} = Z_{\odot}$ (iii) CNO-enhanced case, with $X/Y = (X/Y)_{\odot}$ and $Z_{\text{CNO}} = 4 Z_{\odot}$, where the metallicity is composed of ^{14}O and ^{15}O in the ratio of mass fractions 7 : 13 (Hanawa et al. 1983). Furthermore, we partially simulate additional metallicity cases, $Z_{\text{CNO}}/Z_{\odot} = 2$ and 3.3.

To minimize the influence of compositional inertia (Woosley et al. 2004), we prepare the XRB initial conditions by calculating the steady state with compressional heating (Dohi et al. 2021). We discard the first 20 burst events for the early clocked phase and the first event for the later NinjaSat phase. For the surface boundary, we adopt the radiative-zero boundary condition at $M_r/M_{\text{NS}} = 10^{-16}$ for most cases (Paczynski 1983)². Note that this condition tends to be relaxed during the NinjaSat phase because the burst calculations become highly unstable.

3 Results

We calculate XRB models with the HERES code for the different sets of $(X/Y, Z_{\text{CNO}}, \dot{M}_{-9})$, as described in the previous section. We compare the calculations of light curves in two different phases: (i) the early clocked burster phase (in Section 3.1) observed by INTEGRAL, NinjaSat, and NICER (Ng et al. 2024) and (ii) the decline phase of persistent luminosity (in Section 3.2) only observed by NinjaSat (Takeda et al. 2025).

3.1 The clocked burst phase (early phase)

The calculated recurrence time Δt and burst decay time τ_e are compared with that of SRGA J1444 in figure 2, where we adopt the observed values reported by Sanchez-Fernandez et al. (2024) as reference. In general, a lower X/Y ratio ($0.5(X/Y)_{\odot}$, He enhanced) and/or a higher Z_{CNO} decrease τ_e . For $\dot{M}_{-9} = 3$, most $0.5(X/Y)_{\odot}$ models, except those with $Z_{\text{CNO}} = Z_{\odot}$, closely reproduce the observations. In particular, the metal-rich models with $Z_{\text{CNO}} = 4 Z_{\odot}$ are favored compared to other compositions. In contrast, for higher mass accretion $\dot{M}_{-9} = 4$, all cases show a shorter Δt , with $X/Y = 0.5(X/Y)_{\odot}$ and $Z_{\text{CNO}} = Z_{\odot}$ providing the closest match to the observations. In summary, the solar composition cases ($(X/Y)_{\odot}$ and $Z_{\text{CNO}} = Z_{\odot}$) across all mass accretion rates appear unlikely to reproduce the observed values.

The comparison of light curve profiles also indicates a non-solar composition, as shown in figure 3: calculated light curves are plotted along with the NICER observation. In the solar composition case (figure 3a), values remain elevated from the peak through the tail due to nuclear heating from burning residual hydrogen (Wallace & Woosley 1981; Hanawa & Fujimoto 1984), as observed in bursts of the clocked burster GS 1826–24 (Heger et al. 2007). This suggests that SRGA J1444 may have a significantly lower remaining hydrogen abundance (X) after the rp -process, compared to previous bursters, probably due to an initially lower X/Y ratio. In fact, the lower X/Y models (figure 3b,c) closely

² In the clocked burster phase, we confirm that the light curves are unchanged between $M_r/M_{\text{NS}} = 10^{-16}$ and $M_r/M_{\text{NS}} = 10^{-19}$, latter of which is taken in our previous calculation (e.g., Dohi et al. 2021)

¹ <https://reaclib.jinaweb.org>

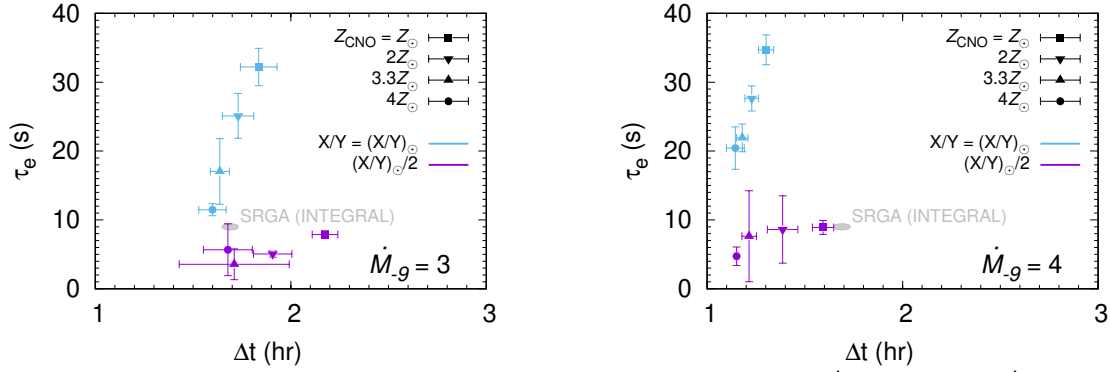


Fig. 2. Calculated Δt and τ_e with several X/Y and Z_{CNO} values for different mass accretion rates, $\dot{M}_{-9} = 3$ (left), and $\dot{M}_{-9} = 4$ (right). The model errors are represented by the 1σ error. The gray area with “SRGA (INTEGRAL)” indicates the reported value by Sanchez-Fernandez et al. 2024, assuming relative errors, 5% for Δt and 10% for τ_e .

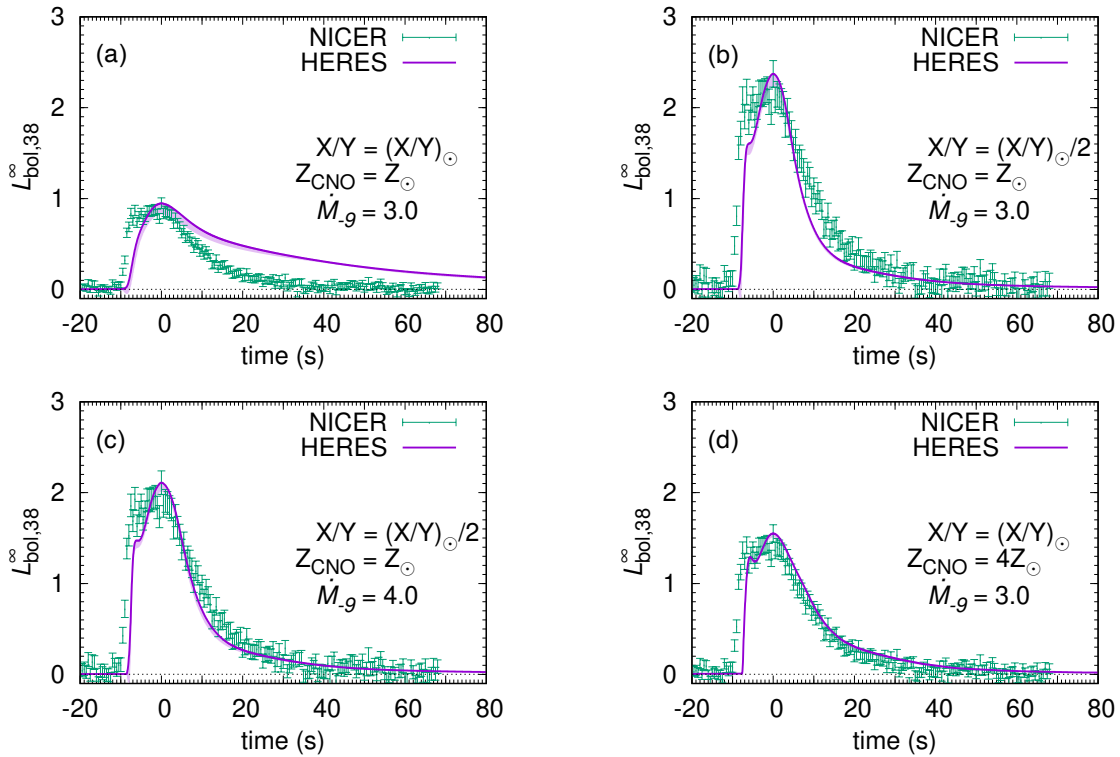


Fig. 3. Simulated light curves with different X/Y , Z , and \dot{M}_{-9} compared with NICER observations (Ng et al. 2024). (a) the solar composition, (b,c) He-enhanced case, and (d) CNO-enhanced case.

match the observed light curve features after the peak.

The CNO-enhanced case (figure 3d) appears to reproduce the double-peak structure more effectively than the low X/Y model. This double-peak structure may result from abundant hot CNO cycle seeds, as shown in Lampe et al. 2016; Song et al. 2024. As the time scale for the luminosity increase shortens, the synthesis of the initial waiting point, ^{56}Ni , occurs earlier. Consequently, the rapid luminosity increase is moderated despite the increase in temperature in the ignition layer. Eventually, the luminosity reaches its peak, which is affected by the temporary stagnation of the r-process before transitioning into the tail phase.

3.2 The decline phase (later phase)

For the later phase of SRGA J1444, we adopt the last two burst profiles of the calculation, where the accretion rate is lower by a factor of ~ 4 than other X-ray observations, as seen in figure 1. To derive the bolometric luminosity from the count rate values, we scale the data to align the 2nd peak luminosity closely with the observed values. To fit the observed short rise time, we shift the original observational data to the left by 5 seconds. In the case of SRGA J1444, this treatment is justified according to Molkov et al. (2024); time evolution of count rates and bolometric flux, which are presented in figures 3 and 4 of Molkov et al. (2024), respectively, show similar behavior, implying weak energy dependence on the energy conversion factor (see also figures 2 and 3 in Ng et al. 2024).

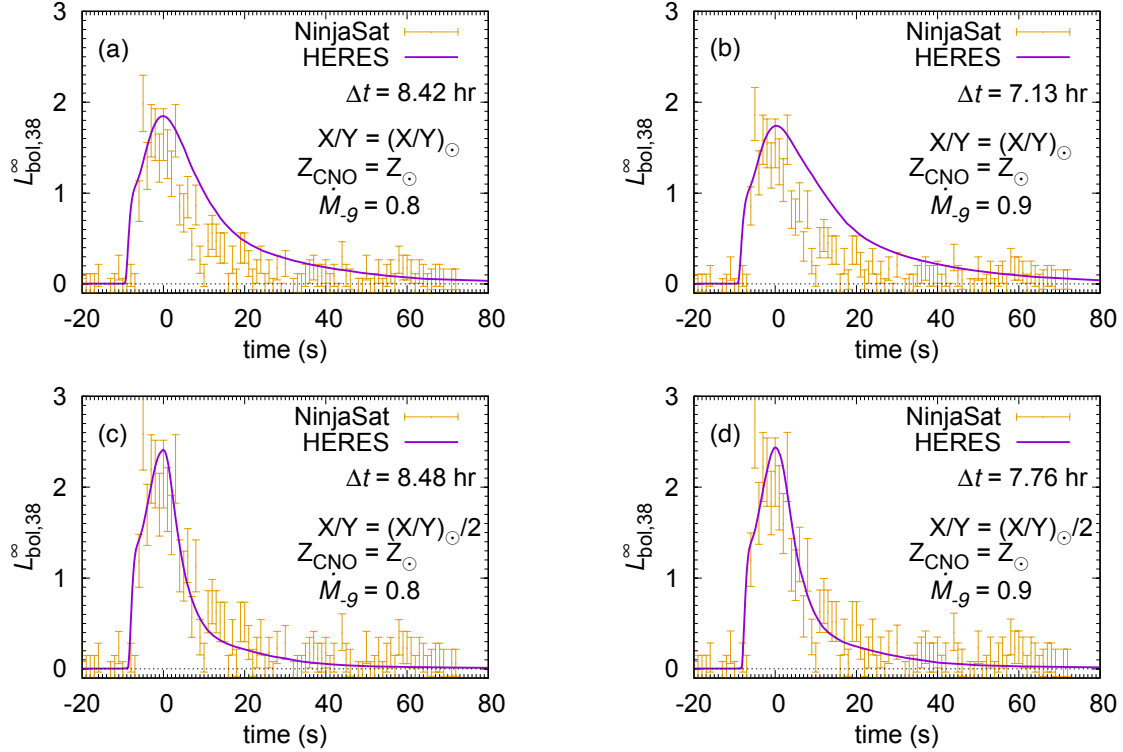


Fig. 4. Simulated light curves overplotted on observations by NinjaSat: (a,b) solar composition, (c,d) He-enhanced case.

Figure 4 shows the results of simulated light curves along with observations by NinjaSat. The solar composition model (figure 4a and 4b) has a longer burst duration than the observation. On the other hand, the He-enhanced model $X/Y = (X/Y)_{\odot}/2$ (figures 4c and 4d), which has a shorter duration, shows better agreement. In particular, if we take $\dot{M}_{-9} = 0.9$ (figure 4d), the corresponding recurrence time is $\Delta t = 7.76$ h, close to the NinjaSat observation of $\Delta t = 7.909$ h. Note that this He-enhanced model agrees with INTEGRAL and NICER with $\dot{M}_{-9, \text{clocked}} = 4$, which satisfies the constraint from persistent flux observations, equation (2), in case of $\dot{M}_{-9, \text{NinjaSat}} = 4$. Thus, He-enhanced cases with solar metallicity, i.e., $X/Y \simeq (X/Y)_{\odot}/2$ and $Z_{\text{CNO}} \simeq Z_{\odot}$, are preferred by SRGA J1444 observations.

Regarding the metal-rich case with $Z_{\text{CNO}} = 4 Z_{\odot}$, we conducted XRB calculations with $\dot{M}_{-9} = 0.8$ and 0.9 , both of which failed after the first XRB reached peak luminosity due to the hydrostatic limitations of HERES. This failure implies the onset of photospheric radius expansion, which was, however, *not* observed by NinjaSat. Additionally, if we approximate the time since the start of the simulation to the first burst (when the simulation fails) as a lower limit to the recurrence time (see also Matsuo et al. 2011 for a pure He-burning case), our HERES models predict $\Delta t = 25$ h and 12 h for $\dot{M}_{-9} = 0.8$ and 0.9 , respectively—both substantially longer than the observed Δt . Physically, this results from the extended duration of the hot CNO cycle, which efficiently consumes hydrogen that was supposed to be a fuel, sustained by a high abundance of CNO seeds. The low \dot{M}_{-9} model, representative of a cooler environment, struggles to transition into a hot bi-CNO cycle through α capture on ^{14}O and ^{15}O . Consequently, the hot CNO cycle could persist for an extended duration, a scenario considered in Liu et al. (2017) in relation to the extra heating source of MAXI J0556–332.

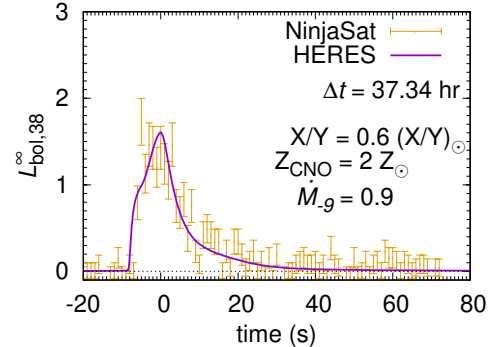


Fig. 5. The marginally HeCNO-enhanced case with $X/Y = 0.6 (X/Y)_{\odot}$, $Z_{\text{CNO}} = 2 Z_{\odot}$, and $\dot{M}_{-9} = 0.9$.

We also consider cases where both He and CNO elements are enhanced. For example, we perform XRB calculations with $X/Y = 0.6 (X/Y)_{\odot} = 1.75$ and $Z_{\text{CNO}} = 2 Z_{\odot}$, representing a marginally HeCNO-enhanced scenario compared to our purely He- or CNO-enhanced models. During the clocked burster phase, this model produces results similar to the He-enhanced case, aligning well with INTEGRAL and NICER observations at $\dot{M}_{-9} = 3.5$. In the decline phase, we set $\dot{M}_{-9} \lesssim 0.9$ based on equation(2), yielding a light curve that closely matches NinjaSat observations, similar to the He-enhanced scenario (figure 5). However, the recurrence time is too long ($\Delta t \simeq 37$ h) to match the observed 7.9 h due to a temperature low enough to delay the triple- α reaction, prolonging the hydrogen-triggered hot CNO cycle³. In short, the

³ At high \dot{M}_{-9} , the triple- α reaction initiates due to elevated temperature, without delay from the hydrogen-triggered hot CNO cycle. Testing the same

HeCNO-enhanced case, like the CNO-enhanced one, seems unfavorable because hydrogen accumulation needed for the XRB is difficult in low mass accretion scenarios for accreting NSs.

In summary, while various combinations of He and metal enhancement can replicate both the light curve profile and recurrence time during the clocked burster phase, increasing metallicity beyond the solar level tends to extend the recurrence time in the decline phase well beyond observed values. Thus, our current simulations by HERES suggest that a helium-enhanced scenario is the most favorable for explaining the full range of observations by INTEGRAL, NICER, and NinjaSat.

4 Summary and discussion

In the present study, we calculated XRB models with the HERES code to investigate the behavior of the recently observed clocked burster SRGA J1444. By calculating with a wide range of model parameters, we have identified appropriate XRB model configurations that align with the recent multiple X-ray observations, such as the decay time (e-folding time) and recurrence time observed by INTEGRAL and the light curve profiles observed by NICER and NinjaSat. In particular, the short decay time and the plateau structure can be reproduced with He-enhanced models with $X/Y = 1.5$, where rp-process heating is weaker. In this case, the corresponding accretion rate is obtained as $\dot{M}_{-9} \approx 3\text{--}4$ for the clocked phase, while $\dot{M}_{-9} \approx 0.8\text{--}0.9$ for the decline phase where the last two bursts were observed by NinjaSat.

The discovery of helium-enhanced XRBs provides valuable constraints on the preceding evolutionary history of the binary system. Specifically, it allows us to distinguish between channels that have descended from the intermediate mass X-ray binary as opposed to systems that had low-mass companions from birth (Podsiadlowski et al. 2002). In the intermediate mass X-ray binary scenario, the outer layers of an initially $\gtrsim 2 M_{\odot}$ star are stripped to expose deeper layers that used to be part of the convective core. Such layers will have elevated He abundances as well as CNO-processed metal abundances. In contrast, the low-mass X-ray binary scenario would predict the donor's surface composition to be similar to its primordial composition (Kalogera & Webbink 1996). It is the donor's surface material that accretes onto the NS, so it is clear that the two scenarios predict distinct accretion compositions. For the case of SRGA J1444, we constrain the hydrogen to helium ratio to be $X/Y \sim 1.5$, corresponding to $X \sim 0.6$ and $Y \sim 0.4$. This is sufficiently helium-enriched compared to the solar composition ($Y \sim 0.23\text{--}0.28$), supporting the intermediate mass X-ray binary scenario.

Together with other observational constraints, we can further constrain the companion star's birth mass. Since SRGA J1444 is an X-ray pulsar, the mass function (relation between NS mass, its companion mass, and inclination angle) is known through pulsar timing models (Ng et al. 2024). The inclination angle has been measured to be $i = 74.1_{-6.3}^{+5.8} \text{ }^{\circ}$ by recent IXPE's polarization observation. Combining these mass function and inclination angle constraints and assuming an NS mass of $M_{\text{NS}} \gtrsim 1.2 M_{\odot}$, we expect the current donor mass to be $M_{\text{don}} \sim 0.3\text{--}0.4 M_{\odot}$. Given that our XRB modeling indicates a modest but non-negligible deviation of the composition of the accreted matter from the solar value, we can infer that the current donor mass is just slightly

smaller than the mass of the convective core at the zero-age main sequence ($M_{\text{conv},0}$), below which the composition becomes increasingly He-enhanced. Based on analytic models of convective core evolution (Shikauchi et al. 2024), we expect the mass difference to be within $1 < M_{\text{don}}/M_{\text{conv},0} \lesssim 1.1$. Therefore, the initial convective core mass of the donor should have been slightly larger than the current donor mass $M_{\text{conv},0} \sim 0.3\text{--}0.5 M_{\odot}$, roughly corresponding to an initial stellar mass of $M_{\text{don},0} \sim 2\text{--}2.5 M_{\odot}$. These constraints can be further improved with more observations and detailed modeling, e.g., by comparing the radii of such partially stripped stars in detailed models and the observationally inferred Roche lobe size of the donor.

The high- Z_{CNO} scenario in our simulations results in a longer recurrence time ($\Delta t = 25$ h for $\dot{M}_{-9} = 0.8$ and $\Delta t = 12$ hr for $\dot{M}_{-9} = 0.9$) compared to the NinjaSat observation, which shows $\Delta t \simeq 7.9$ hr, suggesting an inconsistency. However, the recurrence time is significantly affected by the efficiency of the hot CNO cycle due to the presence of numerous CNO seeds, which is particularly sensitive to the *bottleneck* reactions $^{14}\text{O}(\alpha, p)^{17}\text{F}$ and $^{15}\text{O}(\alpha, \gamma)^{19}\text{Ne}$ (e.g., Fisker et al. 2008; Meisel et al. 2019). Thus, if the recurrence time Δt can be shortened by reaction rate uncertainties (and possibly other model parameters), the high- Z_{CNO} scenario may not be entirely ruled out. Should the true reaction rates be higher than those used in the present study, which is plausible due to the absence of strict upper limits, the hot CNO cycle could proceed on a shorter timescale, thereby decreasing Δt . Furthermore, the simulated light curves during the clocked-burst phases match the observed features well, including the double-peak structure (see also discussion in Song et al. 2024).

Astronomically, the question arises whether stars with such high metallicities exist in the Galactic outer disc region. Such high- Z stars are commonly identified in the Galactic inner disc region (Hayden et al. 2015), suggesting such stars may have migrated outward. Tsujimoto (2021) discusses the possibility of even further high metallicity stars $\sim 10 Z_{\odot}$ in the Galactic bulge transfer to the Solar system neighbor. Additionally, relaxing the stringent requirements for metal abundance would present a more frequent scenario. Therefore, further investigation into the high- Z scenario for SRGA J1444 still remains worthwhile from both nuclear physics and astrophysics perspectives.

In this study, we assume a canonical NS mass value of $1.4 M_{\odot}$. However, we note that the exact value of the NS mass affects our constraints on the composition of X/Y and X_{CNO} in accreting matter. As observational binary parameters of SRGA J1444 improve, the NS mass estimate should become more precise. In fact, a significantly higher NS mass, potentially exceeding $2 M_{\odot}$, is suggested by Takeda et al. (2025)–based on the flat-disk assumption (Fujimoto 1988) and $\xi_b/\xi_p \simeq 0.71$, derived by the IXPE observation (Papitto et al. 2024)⁴. Further investigation of SRGA J1444 XRB events across different NS masses is desirable, especially in the case of massive NSs.

The analyses done in this Letter crucially hinge on the measurement of Δt in the decline phase made by NinjaSat. Such persistent monitoring was only possible due to the flexibility in operations unique to small CubeSat satellites. These results demonstrate just a portion of the rich science that can be achieved from small-scale satellite observations in the future.

⁴ This is due to a higher gravitational redshift, z_g , with $\xi_b/\xi_p \propto 1 + 1/z_g$ (see Section 6.4 in Meisel 2018). However, the mass dependence of ξ_b/ξ_p is likely more complex due to neutron star microphysics (Dohi et al. 2021). Therefore, the correlation between the NS mass and the η parameter in equation (1) (Dohi et al. 2024) is essential for accurately determining NS mass.

composition at $\dot{M}_{-9} = 1$ (unlikely for SRGA J1444 by equation (2)) yields $\Delta t = 6.16$ h, suggesting a critical \dot{M}_{-9} between 0.9 and 1 that affects whether the hot CNO cycle quickly stabilizes in equilibrium.

Acknowledgments

The authors thank H.L. Liu, S. Nagataki, Ph. Podsiadlowski, and T. Tsujimoto for their valuable discussions. This project was financially supported by JSPS KAKENHI (JP20H05648, JP21H01087, JP23KJ1964, JP23K19056, JP24H00008). N.N. received support from the RIKEN Intensive Research Project (FY2024-2025). Part of the computations in this work were performed using the computer facilities at CfCA in NAOJ and YITP at Kyoto University.

References

Aranzana, E., Sánchez-Fernández, C., & Kuulkers, E. 2016, *A&A*, 586, A142

Bult, P., et al. 2022, *ApJL*, 935, L32

Cocchi, M., Bazzano, A., Natalucci, L., Ubertini, P., Heise, J., Kuulkers, E., & in 't Zand, J. J. M. 2001, *Advances in Space Research*, 28, 375

Cornelisse, R., et al. 2003, *A&A*, 405, 1033

Dohi, A., Hashimoto, M.-a., Yamada, R., Matsuo, Y., & Fujimoto, M. Y. 2020, *Progress of Theoretical and Experimental Physics*, 2020, 033E02

Dohi, A., Iwakiri, W. B., Nishimura, N., Noda, T., Nagataki, S., & Hashimoto, M. 2024, *ApJ*, 960, 14

Dohi, A., Nakazato, K., Hashimoto, M.-a., Yasuhide, M., & Noda, T. 2019, *Progress of Theoretical and Experimental Physics*, 2019, 113E01

Dohi, A., Nishimura, N., Hashimoto, M., Matsuo, Y., Noda, T., & Nagataki, S. 2021, *ApJ*, 923, 64

Dohi, A., Nishimura, N., Sotani, H., Noda, T., Liu, H.-L., Nagataki, S., & Hashimoto, M. 2022, *ApJ*, 937, 124

Fiocchi, M., Bazzano, A., Bruni, G., Ludlam, R., Natalucci, L., Onori, F., & Ubertini, P. 2019, *ApJ*, 887, 30

Fisker, J. L., Schatz, H., & Thielemann, F.-K. 2008, *ApJS*, 174, 261

Fujimoto, M. Y. 1988, *ApJ*, 324, 995

Fujimoto, M. Y., Hanawa, T., Iben, I., J., & Richardson, M. B. 1984, *ApJ*, 278, 813

Galloway, D. K., Cumming, A., Kuulkers, E., Bildsten, L., Chakrabarty, D., & Rothschild, R. E. 2004, *ApJ*, 601, 466

Galloway, D. K., Goodwin, A. J., & Keek, L. 2017, *PASA*, 34, e019

Galloway, D. K., et al. 2020, *ApJS*, 249, 32

Haensel, P., & Zdunik, J. L. 2008, *A&A*, 480, 459

Hanawa, T., & Fujimoto, M. Y. 1984, *PASJ*, 36, 199

Hanawa, T., Sugimoto, D., & Hashimoto, M. A. 1983, *PASJ*, 35, 491

Hayden, M. R., et al. 2015, *ApJ*, 808, 132

Heger, A., Cumming, A., Galloway, D. K., & Woosley, S. E. 2007, *ApJL*, 671, L141

Hu, J., et al. 2021, *Phys. Rev. Lett.*, 127, 172701

Johnston, Z., Heger, A., & Galloway, D. K. 2020, *MNRAS*, 494, 4576

Kalogera, V., & Webbink, R. F. 1996, *ApJ*, 458, 301

Lam, Y. H., Liu, Z. X., Heger, A., Lu, N., Jacobs, A. M., & Johnston, Z. 2022a, *ApJ*, 929, 72

Lam, Y. H., Lu, N., Heger, A., Jacobs, A. M., Smirnova, N. A., Nieto, T. K., Johnston, Z., & Kubono, S. 2022b, *ApJ*, 929, 73

Lampe, N., Heger, A., & Galloway, D. K. 2016, *ApJ*, 819, 46

Li, Z., et al. 2024, *The Astronomer's Telegram*, 16548, 1

Liu, H., Matsuo, Y., Hashimoto, M.-a., Noda, T., & Fujimoto, M. Y. 2017, *Journal of the Physical Society of Japan*, 86, 123901

Matranga, M., et al. 2017, *A&A*, 603, A39

Matsuo, Y., Tsujimoto, H., Noda, T., Saruwatari, M., Ono, M., Hashimoto, M., & Fujimoto, M. Y. 2011, *Progress of Theoretical Physics*, 126, 1177

Meisel, Z. 2018, *ApJ*, 860, 147

Meisel, Z., Deibel, A., Keek, L., Shternin, P., & Elfriz, J. 2018, *Journal of Physics G Nuclear Physics*, 45, 093001

Meisel, Z., Merz, G., & Medvid, S. 2019, *ApJ*, 872, 84

Mihara, T., et al. 2024, *The Astronomer's Telegram*, 16469, 1

Molkov, S. V., et al. 2024, *arXiv e-prints*, arXiv:2404.19709

Ng, M., et al. 2024, *ApJL*, 968, L7

Paczynski, B. 1983, *ApJ*, 267, 315

Papitto, A., et al. 2024, *arXiv e-prints*, arXiv:2408.00608

Podsiadlowski, Ph., Rappaport, S., & Pfahl, E. D. 2002, *ApJ*, 565, 1107

Sanchez-Fernandez, C., Kuulkers, E., Ferrigno, C., & Chenevez, J. 2024, *The Astronomer's Telegram*, 16485, 1

Shikauchi, M., Hirai, R., & Mandel, I. 2024, *arXiv e-prints*, arXiv:2409.00460

Song, L., Liu, H., Zhu, C., Zhen, G., Lü, G., & Xu, R. 2024, *MNRAS*

Takeda, T., et al. 2025, in preparation.

—. 2024, *The Astronomer's Telegram*, 16495, 1

Togashi, H., Nakazato, K., Takehara, Y., Yamamuro, S., Suzuki, H., & Takano, M. 2017, *Nucl. Phys. A*, 961, 78

Tsujimoto, T. 2021, *ApJL*, 920, L32

Ubertini, P., Bazzano, A., Cocchi, M., Natalucci, L., Heise, J., Muller, J. M., & in 't Zand, J. J. M. 1999, *ApJL*, 514, L27

Wallace, R. K., & Woosley, S. E. 1981, *ApJS*, 45, 389

Wijnands, R., Parikh, A. S., Altamirano, D., Homan, J., & Degenaar, N. 2017, *MNRAS*, 472, 559

Woosley, S. E., et al. 2004, *ApJS*, 151, 75

Zhen, G., Lü, G., Liu, H., Dohi, A., Nishimura, N., Zhu, C., Song, L., Wang, W., & Xu, R. 2023, *ApJ*, 950, 110

Appendix 1 Characteristic quantities of XRB light curves

The burst light curves are characterized by several parameters, such as recurrence time (Δt), total burst energy in units of 10^{39} erg ($E_{b,39}$), peak luminosity in units of 10^{38} erg s $^{-1}$ ($L_{pk,38}$), and e-folding time (τ_e). In table 1 and 2, we list their values with 1σ errors in a number of burst profiles (n_{anal}) for the solar composition case ($X/Y = 2.9$ and $Z_{CNO} = 0.015$) and the He-enhanced case ($X/Y = 1.5$ and $Z_{CNO} = 0.015$), respectively. These values were utilized in Takeda et al. (2025) for comparison with observational data.

| \dot{M}_{-9} | n_{anal} | Δt [h] | $E_{b,39}$ | $L_{pk,38}$ | τ_e [s] |
|----------------|------------|-----------------|-----------------|-----------------|----------------|
| ... 0.8 | 1 | 8.42 | 4.12 | 2.37 | 6.3 |
| 0.9 | 1 | 7.13 | 4.70 | 1.74 | 2.2 |
| 1 | 1 | 6.85 | 4.36 | 2.41 | 11.2 |
| 2 | 37 | 2.97 ± 0.15 | 4.24 ± 0.16 | 1.13 ± 0.20 | 30.9 ± 4.8 |
| 2.5 | 61 | 2.30 ± 0.09 | 4.20 ± 0.18 | 1.04 ± 0.14 | 31.8 ± 2.9 |
| 3 | 163 | 1.84 ± 0.09 | 4.04 ± 0.19 | 0.95 ± 0.12 | 32.6 ± 2.8 |
| 4 | 220 | 1.30 ± 0.04 | 3.63 ± 0.16 | 0.81 ± 0.05 | 34.5 ± 2.2 |
| 5 | 221 | 0.97 ± 0.05 | 3.11 ± 0.20 | 0.71 ± 0.06 | 34.4 ± 2.2 |

Table 1. Several burst characteristics with solar compositions.

| \dot{M}_{-9} | n_{anal} | Δt [h] | $E_{b,39}$ | $L_{pk,38}$ | τ_e [s] |
|----------------|------------|-----------------|-----------------|-----------------|----------------|
| 0.8 | 1 | 8.48 | 3.38 | 2.41 | 6.2 |
| 0.9 | 1 | 7.76 | 3.63 | 2.44 | 7.4 |
| 1 | 1 | 6.61 | 3.82 | 2.39 | 7.6 |
| 2 | 19 | 3.37 ± 0.07 | 3.92 ± 0.07 | 2.68 ± 0.07 | 4.6 ± 0.7 |
| 2.5 | 25 | 2.67 ± 0.23 | 3.94 ± 0.10 | 2.68 ± 0.23 | 7.2 ± 1.1 |
| 3 | 96 | 2.17 ± 0.07 | 3.82 ± 0.11 | 2.37 ± 0.16 | 7.9 ± 0.6 |
| 4 | 35 | 1.59 ± 0.05 | 3.62 ± 0.16 | 2.11 ± 0.10 | 8.9 ± 1.0 |
| 5 | 126 | 1.13 ± 0.07 | 3.08 ± 0.19 | 1.58 ± 0.34 | 12.3 ± 4.9 |

Table 2. Several averaged burst characteristics with He enhanced case.